IEEE Access
Multidisciplinary | Rapid Review | Open Access Journal

Received November 21, 2021, accepted December 9, 2021, date of publication December 13, 2021,
date of current version December 29, 2021.

Digital Object Identifier 10.1109/ACCESS.2021.3134911

Position Fault Detection for UAM Motor With Seamless Transition

TAEYEON LEE[1], HEEKWANG LEE[2], POOREUM JANG[1], YUNKYUNG HWANG[1], AND KWANGHEE NAM[1], (Life Member, IEEE)
[1]Department of Electrical Engineering, Pohang University of Science and Technology (POSTECH), Pohang 37673, South Korea
[2]Hyundai Motor R&D Center, Uiwang-si 16082, South Korea

Corresponding author: Kwanghee Nam (kwnam@postech.ac.kr)

ABSTRACT A strict fault tolerance is required in urban air mobility (UAM). The motor position sensor is one of the monitoring targets in UAMs, because it is in a harsh environment such as rain, ice, dust, vibration, etc. In this work, a resolver-based sensor method and a sensorless algorithm are fused in cooperative mode. Under normal conditions, the sensored angle and the sensorless angle are weighted equally. However, in case of sensor failure, only the sensorless method is selected. In other cases, only the sensored angle is fully respected. It is assumed here that the sensored method as well as the sensorless method may fail. To determine which of the two methods is faulty, the measured current is used as a reference. The virtual current is obtained by numerically solving the permanent magnet synchronous motor (PMSM) model in the stationary frame using the rotor angles. The position fault is then detected by comparing the virtual current to the measured current. Sigmoid functions with a step at zero are used for fault detection and fusion method robust against sudden error fluctuations or noise. Convincing performance and robustness are demonstrated by simulation and experimental results.

INDEX TERMS Urban air mobility, fault-tolerant control, permanent magnet synchronous motors, motor control, Runge-Kutta 4th.

I. INTRODUCTION

Electric urban air mobility (UAM) envisions a safe, sustainable, and accessible air transportation system for passenger mobility within traversing metropolitan [1]. UAM is gaining increasing attention with advances in battery energy density and fuel cell batteries. In the near future, UAMs will become the main short-haul aircraft due to the convenience of vertical takeoff and landing. Fig. 1 shows the conceptual design of a UAM equipped with four propulsion electric motors. PMSMs are primarily used in UAMs due to their high power density. In PMSM speed control, field-oriented control has an absolute advantage, which requires rotor position [2]. Since high reliability is strongly demanded in aerial vehicle, sensor fault tolerance is also important. The resolver is most widely used in PMSMs since they are robust and provide absolute position [3], [4]. It also provides more accurate angle information by compensating the resolver angle error [5], [6].

Many safety critical systems use multi-sensors in parallel, fusion, and backup to increase fault tolerance. Sensorless methods were often used as a backup for sensor failure in the high reliability system [7]–[13]. Kai *et al.* [7] detected position sensor fault by monitoring the difference between measured and estimated values. G. Foo *et al.* [8] conducted a similar study using the extended Kalman filter (EKF). In [9], a robust fault detection method was proposed using an adaptive EKF with varying covariance. H. Berriri [10] proposed a fault detection method based on parity space

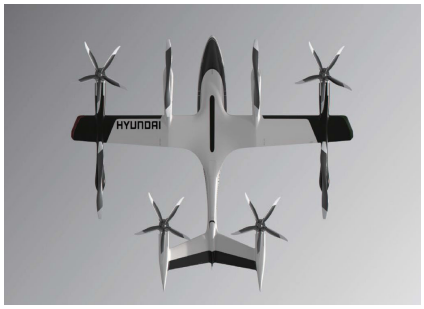

FIGURE 1. A concept design of UAM. (With the courtesy of Hyundai Motor Company).

The associate editor coordinating the review of this manuscript and approving it for publication was N. Prabaharan.

that is less affected by parameter changes. A fault detection method was proposed with a failover scheme by using extended back electromotive (EMF) force [11]. A transition method was considered based on the adaptive threshold angle to avoid unnecessary switching between sensored and sensorless modes [12], [13]. J. Liu *et al.* [14] also proposed a soft transition method by adjusting the linear weights.

Because sensor failure or sensor error was detected based on the sensorless output, previous work is limited in determining the error or estimating the error. Note that sensorless angle estimation is not always correct because there are uncertainties in inductance [15], [16], back EMF coefficient [17], and temperature-related stator coil resistance [18]. The accuracy is also affected strongly by the uncertainty of the voltage drop over semiconductor switches [19], [20].

In this work, currents are used to determine the accuracy of angles. It employs two virtual PMSM models inside a controller. One is utilizing the sensored angle and the other the sensorless angle for the reference frame. The virtual currents are obtained as the model outputs and they are compared with the measured current. Any value closer to the measured current is considered more accurate. Then, the accurate angle is weighted more than the other. Further sigmoid functions are used in fault detection and determining the weights to enhance the robustness and seamless transition.

This paper is organized as follows: The mathematical PMSM model is stated in the stationary frame and the fault detection method is derived in Section II. A position angle fusing method is developed using the current comparison and relative angle difference in Section III. Simulation results are shown along with failsafe control block diagram in Section IV. Finally, the experimental results are analyzed.

II. PMSM MODEL AND FAULT DETECTION METHOD

Interior PMSM is modeled in the stationary $\alpha\beta$ frame as [17]

$$\begin{aligned}\begin{bmatrix} v_\alpha \\ v_\beta \end{bmatrix} &= r_s \begin{bmatrix} i_\alpha \\ i_\beta \end{bmatrix} + \begin{bmatrix} L_\Sigma + L_\Delta \cos 2\theta_e & L_\Delta \sin 2\theta_e \\ L_\Delta \sin 2\theta_e & L_\Sigma - L_\Delta \cos 2\theta_e \end{bmatrix} \frac{d}{dt} \begin{bmatrix} i_\alpha \\ i_\beta \end{bmatrix} \\ &\quad + 2\omega_e L_\Delta \begin{bmatrix} -\sin 2\theta_e & \cos 2\theta_e \\ \cos 2\theta_e & \sin 2\theta_e \end{bmatrix} \begin{bmatrix} i_\alpha \\ i_\beta \end{bmatrix} + \omega_e \psi_m \begin{bmatrix} -\sin\theta_e \\ \cos\theta_e \end{bmatrix} \end{aligned} \tag{1}$$

Then, it is derived in an ordinary differential equation (ODE) form such that

$$\begin{aligned}\frac{d}{dt} \begin{bmatrix} i_\alpha \\ i_\beta \end{bmatrix} &= \frac{1}{L_d L_q} \begin{bmatrix} L_\Sigma - L_\Delta \cos 2\theta_e & -L_\Delta \sin 2\theta_e \\ -L_\Delta \sin 2\theta_e & L_\Sigma + L_\Delta \cos 2\theta_e \end{bmatrix} \\ &\quad \times \Big(\begin{bmatrix} v_\alpha \\ v_\beta \end{bmatrix} - r_s \begin{bmatrix} i_\alpha \\ i_\beta \end{bmatrix} - 2\omega_e L_\Delta \begin{bmatrix} -\sin 2\theta_e & \cos 2\theta_e \\ \cos 2\theta_e & \sin 2\theta_e \end{bmatrix} \begin{bmatrix} i_\alpha \\ i_\beta \end{bmatrix} \\ &\quad - \omega_e \psi_m \begin{bmatrix} -\sin\theta_e \\ \cos\theta_e \end{bmatrix} \Big), \end{aligned} \tag{2}$$

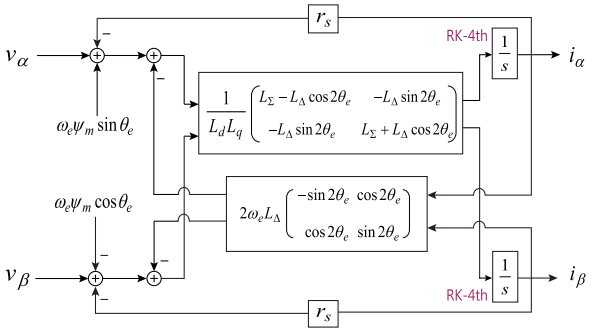

FIGURE 2. The mathematical PMSM modeled in the stationary frame.

where v_α, v_β and i_α, i_β are the $\alpha\beta$-axis voltages and currents. r_s is the stator resistance, $L_\Sigma = \frac{L_d + L_q}{2}$ and $L_\Delta = \frac{L_d - L_q}{2}$ are the average and difference inductances, respectively. Note that if $L_\Delta = 0$, it becomes an surface PMSM model. ψ_m is the PM flux linkage, and θ_e and ω_e are the electrical angle and speed of the rotor. Fig. 2 shows a PMSM block diagram in the stationary frame.

A. TWO SENSED ANGLES FROM SENSORED AND SENSORLESS METHOD

Fig. 3 shows the resolver and its signal processing diagram. It is similar to transformer in structure. It has three winding sets: one is for field excitation and the other two are for signal pickup. The pickup coils are 90° apart, they are called sine and cosine coils. Since the rotor has a flower shape the airgap is nonuniform. Thereby, the carrier is modulated depending on the rotor position. To detect the rotor position, demodulation is necessary. The detection process contains normally the quadrature PLL [3], [4].

In recent decades, sensorless method of PMSM has been studied [21], [22]. These self-sensing controls include back EMF [23]–[25], active flux [26], State observer type [27] etc. In particular, the sensorless control shows good performance in the medium speed range. Thus, sensorless method has been used in parallel, fusion, and backup to prepare for fault tolerance in the high-reliability system [13].

Under normal circumstances, the sensored method is regarded more accurate than the sensorless method. However, the sensor may breakdown under harsh environments. Even if the sensor does not fail completely, it may operate with a partial failure. In such a situation, the use of sensorless method would be better. On the other hand, the sensorless method may also not work properly. It is assumed here that the sensored method as well as the sensorless method may fail. Therefore, we need a criterion to judge which method is more accurate than the other.

B. PROPOSED FAULT DETECTION METHOD

In this study, we propose to use the motor current as a reference to determine a better sensing method. To do this, we use two mathematical PMSM models and apply the same voltage to the model input as the voltage reference used

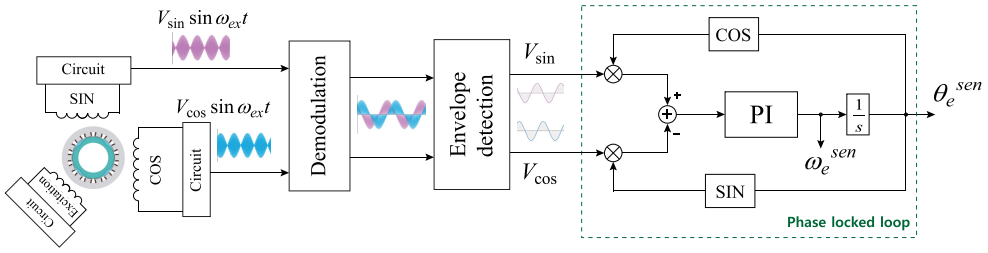

FIGURE 3. Block diagram of resolver demodulation utilizing a quadrature phase locked loop (PLL).

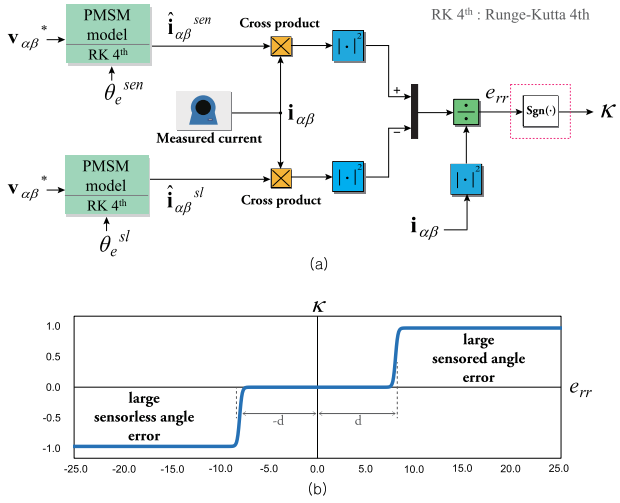

FIGURE 4. (a) Block diagram for fault detection including PMSM models and (b) sigmoid function with a holding region at zero.

for actual current control. The models (2) require the rotor angle. We use the sensored angle θ_e^{sen} for one model and sensorless angle θ_e^{sl} for the other. The motor dynamics are solved by Runge-Kutta 4th method, and the resulting currents are denoted as $\hat{i}_{\alpha\beta}^{sen}$ for a model with θ_e^{sen} and $\hat{i}_{\alpha\beta}^{sl}$ for the other model with θ_e^{sl}.

Fig. 4 (a) shows a block diagram for fault detection. First, the measured current $i_{\alpha\beta}$ is taken cross product with the virtual currents, $\hat{i}_{\alpha\beta}^{sen}$ and $\hat{i}_{\alpha\beta}^{sl}$ such that

$$e_{sen} \equiv i_{\alpha\beta} \otimes \hat{i}_{\alpha\beta}^{sen}, \tag{3}$$

$$e_{sl} \equiv i_{\alpha\beta} \otimes \hat{i}_{\alpha\beta}^{sl}. \tag{4}$$

If θ_e^{sen} is right, then $\hat{i}_{\alpha\beta}^{sen}$ is parallel with $i_{\alpha\beta}$, thereby, $\|e_{sen}\| = 0$. If they are not parallel, $\|e_{sen}\| > 0$. The same is true with the sensorless angle.

Let

$$\begin{aligned} e_{rr} &= \frac{\|e_{sen}\|^2 - \|e_{sl}\|^2}{\|i_{\alpha\beta}\|^2} \\ &= \frac{\|\hat{i}_{\alpha\beta}^{sen}\|^2}{\|i_{\alpha\beta}\|^2} \sin^2(\theta_e - \theta_e^{sen}) - \frac{\|\hat{i}_{\alpha\beta}^{sl}\|^2}{\|i_{\alpha\beta}\|^2} \sin^2(\theta_e - \theta_e^{sl}). \end{aligned} \tag{5}$$

In Fig. 4 (a), normalization is used to make the fault detection free from the magnitude of currents, especially when the current is small.

The fault detection rule is set using the sigmoid function κ defined as

$$\kappa(e_{rr}) \equiv \frac{1}{1 + e^{-r(e_{rr}-d)}} - \frac{1}{1 + e^{r(e_{rr}+d)}}, \tag{6}$$

where r and d are parameters that determine the transition rate and offset value, respectively. Fig. 4 (b) shows an example of κ which gives 1 when the error of θ_e^{sen} is large and -1 when the error of θ_e^{sl} is large. Note that the function κ has a step of $2d$ width at zero. Thereby, $\kappa(e_{rr}) = 0$ when both errors of θ_e^{sen} and θ_e^{sl} are small. This is because fault detection is not attempted in the area where both θ_e^{sen} and θ_e^{sl} errors are small. The reason why each corner is smoothed and the zero step is provided is to prevent chattering due to noise in fault detection. Whenever a position error occurs, a large current is generated, and since the PMSM model takes an angle as an input, a large virtual current is calculated. Therefore, there is a signature current for fault detection.

III. FUSING METHOD BY USING WEIGHTS

Denote by θ_e^c the angle of a reference frame for the field oriented control. In determining θ_e^c, both θ_e^{sen} and θ_e^{sl} are fused with weight ρ:

$$\theta_e^c \equiv \rho\theta_e^{sl} + (1-\rho)\theta_e^{sen}, \quad 0 \le \rho \le 1, \tag{7}$$

If the weights change too quickly, change frequently, or react sensitively to small errors, it can actually impair stability. To prevent this, when changing the weights, it is necessary to smooth out the transition and provide a holding region for small errors. Let $\Delta\theta_e \equiv \theta_e^{sl} - \theta_e^{sen}$. Define another sigmoid function of $\Delta\theta_e$ as

$$f(\Delta\theta_e) = \frac{1}{1 + e^{-\nu(|\Delta\theta_e| - \mu)}}, \tag{8}$$

where ν is a coefficient determining the rate of transition and μ is a value that prevents chattering when $\Delta\theta_e$ is small. Fig. 5 shows f for different values of ν. It gives 0 and 1 for small and large $|\Delta\theta_e|$. Note that the holding region enlarges as μ increases, and the transition slope increases as ν. Utilizing f, the weight is determined as

$$\rho = \frac{1}{2}(1 + \kappa(e_{rr}) f(\Delta\theta_e)) \tag{9}$$

For small $|\Delta\theta_e|$ in the holding region, the reference angle is determined simply as the average of θ_e^{sen} and θ_e^{sl} with $\rho = \frac{1}{2}$.

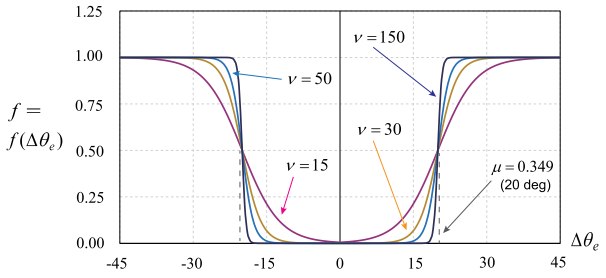

FIGURE 5. Sigmoid function f of angle difference, $\Delta\theta_e$.

If $|\Delta\theta_e|$ is large, either sensorless or sensored angle is selected depending on the sign of κ. Specifically, one of the angle is assumed to be faulty when the relative angle difference is larger than 20°. Note that κ is a function of current error and f is a function of angle relative difference. Both of them have smooth transitions against error variation.

A. PARAMETER DESIGN

Even if a fault does not take place, the angle difference may increase due to acceleration, deceleration, motor parameter variation, PLL delay, etc [13], [15], [28]. Therefore, fault detection should be withheld for naturally occurring errors, and only be activated when a threshold is exceeded. Let $\Delta\theta_{\max}$ be the maximum allowable angle difference. When the angle difference reaches $\Delta\theta_{\max}$, one angle data is considered invalid and the other is chosen alone as $f(\Delta\theta_e) \approx 1$. On the other hand, let $\Delta\theta_{\min}$ be the boundary value of the holding region. Then, the maximum and minimum values of the sigmoid function have the following relationship from the set values $\Delta\theta_{\max}$ and $\Delta\theta_{\min}$:

$$f_{\max} = 1/(1 + e^{-\nu(\Delta\theta_{\max} - \mu)}), \tag{10}$$

$$f_{\min} = 1/(1 + e^{-\nu(\Delta\theta_{\min} - \mu)}), \tag{11}$$

Then, the parameters are obtained such that

$$\nu = \frac{\delta_{\max} - \delta_{\min}}{\Delta\theta_{\max} - \Delta\theta_{\min}}, \tag{12}$$

$$\mu = \frac{\delta_{\max}\Delta\theta_{\min} - \delta_{\min}\Delta\theta_{\max}}{\delta_{\max} - \delta_{\min}}, \tag{13}$$

where

$$\delta_{\max} \equiv \nu(\Delta\theta_{\max} - \mu) = \ln\left(\frac{f_{\max}}{1 - f_{\max}}\right), \tag{14}$$

$$\delta_{\min} \equiv \nu(\Delta\theta_{\min} - \mu) = \ln\left(\frac{f_{\min}}{1 - f_{\min}}\right). \tag{15}$$

IV. SIMULATION RESULTS

Fig. 6 shows a block diagram for speed control of IPMSM. The rotor angles are obtained from a sensor attached to the shaft and from a sensorless algorithm that utilizes stationary voltage ($v^*_{\alpha\beta}$) and current measurements ($i_{\alpha\beta}$). In this work, all three-channel currents are used to eliminate zero-sequence currents and increase the accuracy of the $\alpha\beta$ transformed currents [29]. Note that a resolver and EEMF observer are utilized as the position sensor and the sensorless algorithm, respectively. Two copies of the same Runge-Kutta 4th IPMSM model in the stationary frame are used with the same voltage input. However, the two models use different angles, so they output different virtual currents. To estimate the amount of angle error, the cross product is taken between the virtual currents and the measured current. Based on the relative error e_{rr} of the current vectors, κ is generated, and the weight ρ is obtained using κ and the relative angle error $\Delta\theta_e$. Therefore, angle fusion, fault detection, and failover are possible with the proposed method. In a special case, the current could be zero in standby. To prevent unreliable fault detection when the current magnitudes is less than a noise threshold I_o, a switch is added in Fig. 6. Therefore, the proposed method does not work in near-zero current. In Fig. 6, the input of the sigmoid function, $\Delta\theta$, is preprocessed through LPF. Therefore, it is possible to cope with sudden step angle error through LPF and sigmoid function.

Fig. 7 shows the failover performance when artificial angle errors are injected in the sensored or sensorless angle data. It is assumed that the motor runs at 1000 rpm constant speed and the currents are well controlled based on accurate angle information. However, artificial errors are added to θ_e^{sen} and θ_e^{sl}, and applied to the Runge-Kutta 4th models. Figs. 7 (a) and (b) show altered signals by artificial errors. The relative angle difference between the two angles is shown in Fig. 7 (c). The Runge-Kutta 4th model current, $\hat{i}^{sen}_{\alpha\beta}$ or $\hat{i}^{sl}_{\alpha\beta}$ is not aligned with $i_{\alpha\beta}$ due to the angle error. The corresponding weight ρ and control angle θ_e^c are shown in Figs. 7 (d) and (e). Note that the sensorless signal is selected in interval II with $\rho = 1$ when there is an error in the sensored signal. On the other hand, the sensored signal is selected in interval III with $\rho = 0$ when there is an error in the sensorless signal. However, ρ changes slightly as shown in interval I when the level of error is small.

Fig. 8 shows how the failover algorithm works with motor control. The motor speed is controlled at 1000 rpm. In Fig. 8 (b), the position sensor fails at $t = 2.2$, so that θ_e^{sen} remains the previous data thereafter. Such a fault is detected and the control relies on θ_e^{sl} by changing ρ to 1. Fig. 8 (d) also shows a slight unsettling in the phase currents at the transition. Note however that θ_e^{sl} hits the constant value θ_e^{sen} after one electrical cycle. Then, ρ turns out to be $\frac{1}{2}$ at this point, and goes back to 1 afterwards. For this reason, slight speed ripples are shown in Fig. 8 (a) after the sensor failure with $\theta_e^{sen} = constant$.

Fig. 9 (a) shows a position fault-tolerant control at 500 rpm when the cosine resolver cable is shorted. Thus, the output signal V_{cos} is zero after the fault. Also, this causes θ_e^{sen} to be a rectangular signal. Although these periodic errors increase ripple and distortion in speed and currents, the proposed algorithm works satisfactorily. Fig. 9 (b) shows a similar result when the sine resolver cable is opened. Thus, the value of the

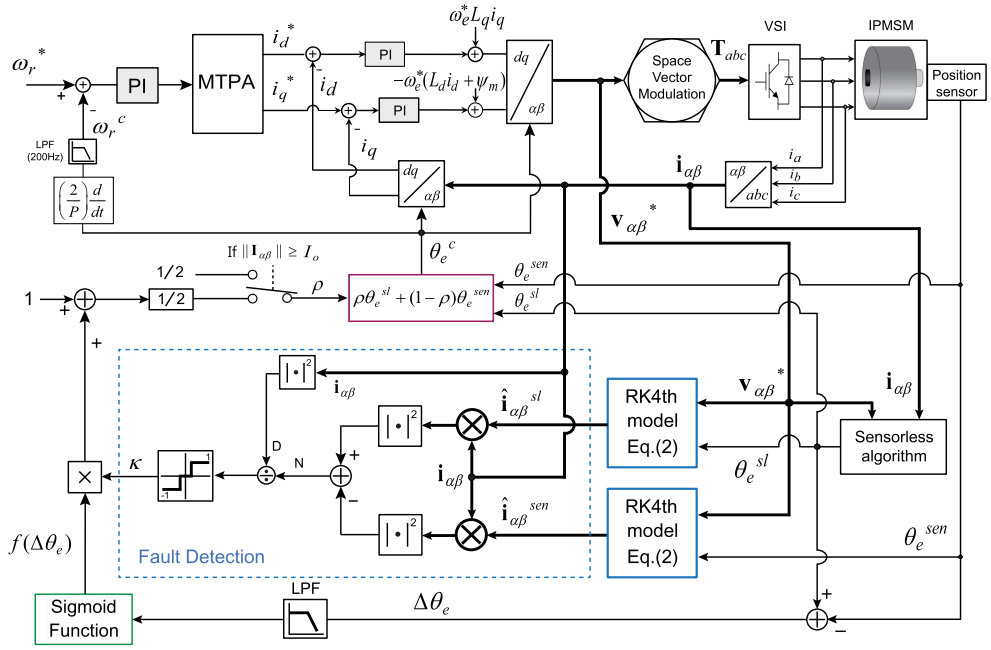

FIGURE 6. Block diagram of failsafe angle sensing algorithm and speed control of PMSM.

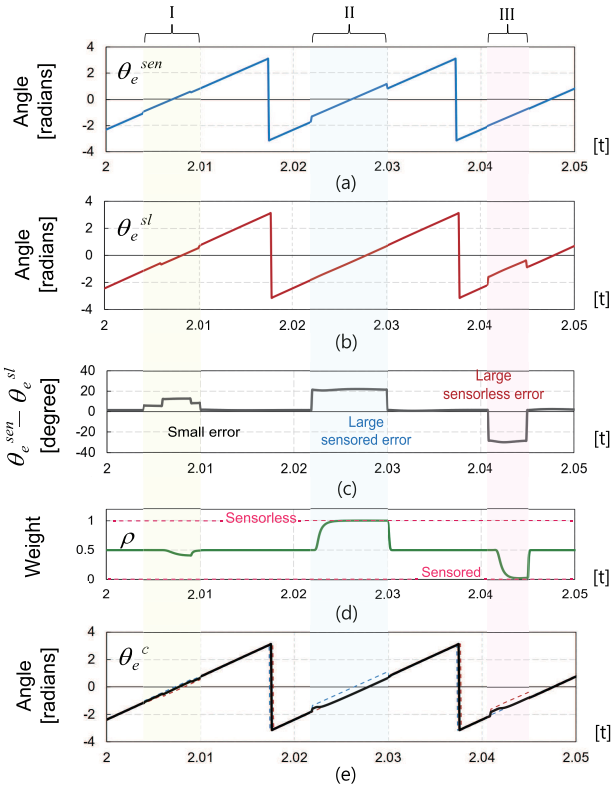

FIGURE 7. Simulation results of angle fusing according to artificial angle error injections at 1000 rpm.

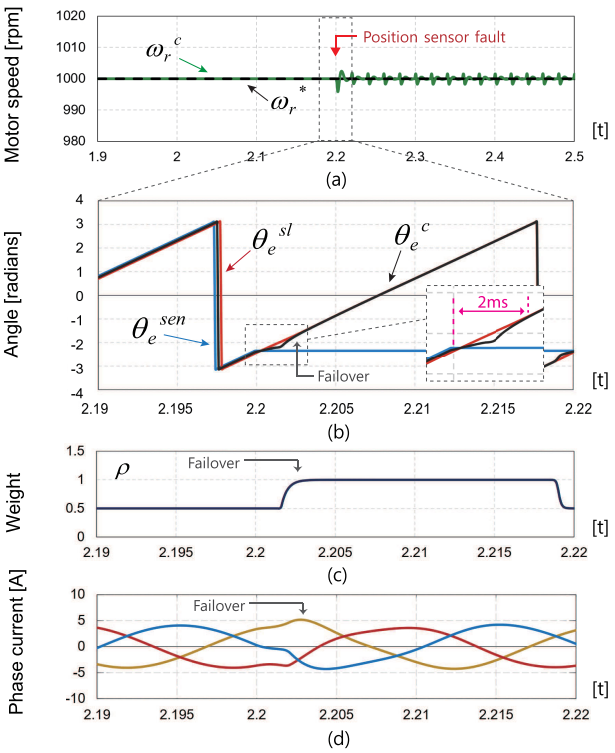

FIGURE 8. Simulation results of angle fusing at 1000 rpm under resolver sensor fault.

output signal V_{sin} is not refreshed after the fault and therefore retains its previous value. In such a case, θ_e^{sen} turns out to be a sinusoidal wave. The algorithm also works satisfactorily.

Fig. 10 shows a simulation of acceleration and deceleration for 0.3 seconds. Fig. 10 (a) shows the result of accelerating from 500 rpm to 1500 rpm and then decelerating back to 500 rpm, and shows the speed difference between

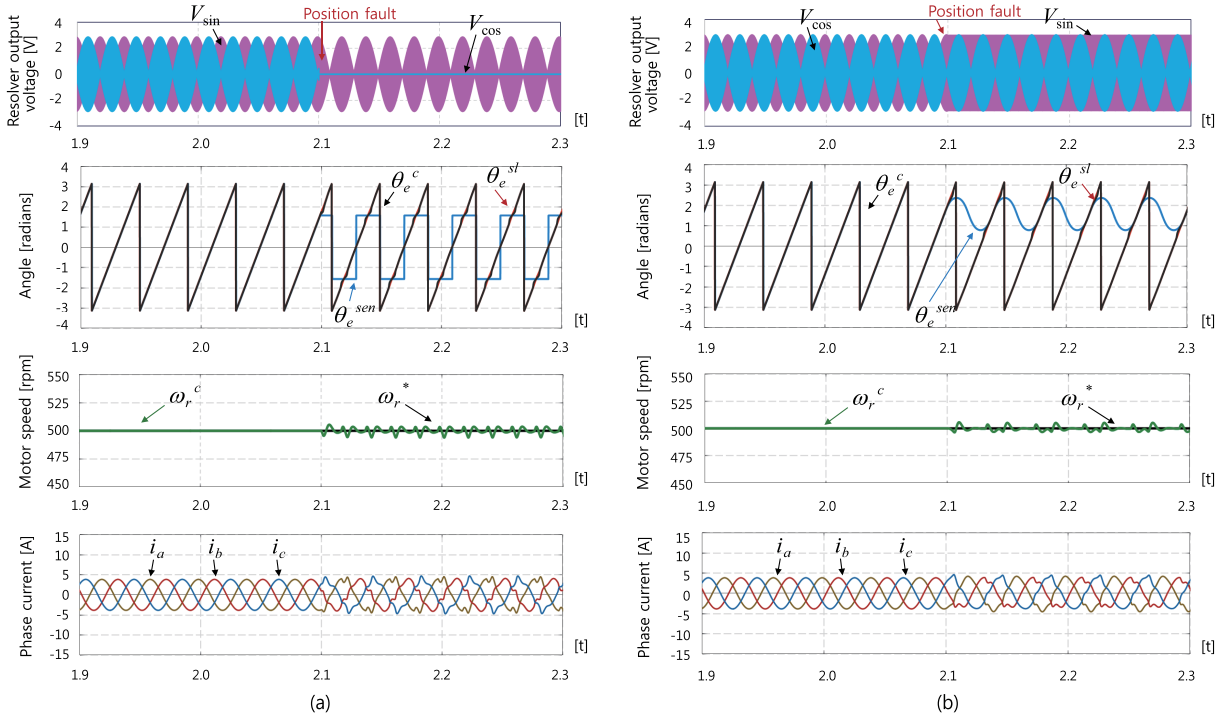

FIGURE 9. Simulation results at 500 rpm under resolver sensor fault: (a) resolver cosine cable short, (b) resolver sine cable open.

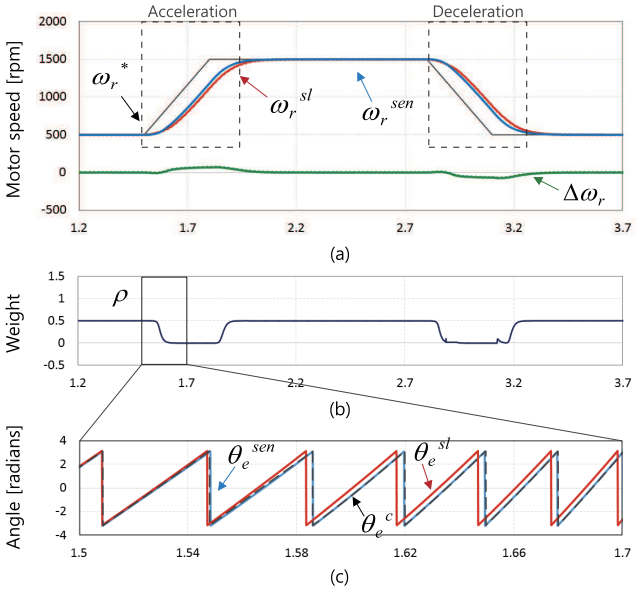

FIGURE 10. Simulation results of acceleration and deceleration in the transient state.

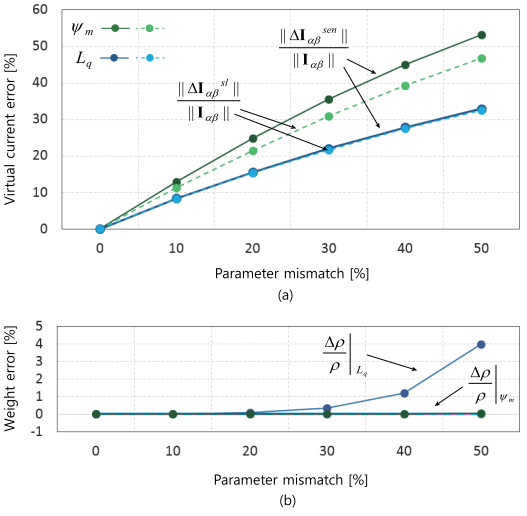

FIGURE 11. Effect of parameter mismatch on PMSM model for virtual current estimation.

sensored and sensorless in the transient state. Since the sensorless method uses a PLL, acceleration/deceleration performance is poor. As shown in Fig. 10 (b), the control angle is smoothly switched to the sensored angle by weight. Similarly, when decelerating, the weights smoothly transition to zero. In Fig. 10 (c), ρ becomes 0 giving a full weight to the sensored method. It is a convincing simulation result that shows the sigmoid function is tuned well in the transients.

Fig. 11 shows current errors and weight variation when the PMSM model involves parameter errors. Fig. 11 (a) shows the virtual current errors for the back EMF constant and q-axis inductance mismatch. When the inductance changes up to 50%, the sensored virtual current changes by about 32.9% and the sensorless virtual current by about 32.5%. When back EMF constant changes up to 50%, the sensored virtual current changes by about 53.2% and the sensorless virtual current by about 46.7%. The virtual current errors increase in proportion to the parameter errors. On the other hand, the change of

TABLE 1. Result of parameter error.

$\Delta L_q/L_q$ [%]	10	20	30	40	50
$\Delta\kappa/\kappa$ [%]	0	0	0	0	0
$\Delta\rho/\rho$ [%]	0.019	0.092	0.337	1.211	4.002
$\Delta\psi_m/\psi_m$ [%]	10	20	30	40	50
$\Delta\kappa/\kappa$ [%]	0	0	0	0	0
$\Delta\rho/\rho$ [%]	0.002	0.006	0.014	0.023	0.056

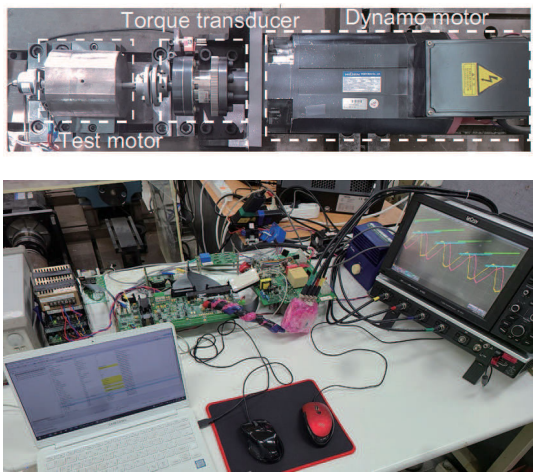

FIGURE 12. Dynamo test bench for experiments.

TABLE 2. Parameters of test IPMSM used in the experiment.

Parameter	Value
Rated output power	1.3 kW
Rated speed	2000 r/min
Rated current	8.7 Arms
Rated line to line voltage	110Vrms
Numbers of poles (P)	4
PM flux linkage constant (ψ_m)	0.11Wb
d-axis inductance (L_d)	6.2mH
q-axis inductance (L_q)	8.6mH
Stator resistance (r_s)	0.3 Ω
PWM switching frequency (f_s)	5000Hz
Sigmoid function $f_{\max}$	0.99
Sigmoid function $f_{\min}$	0.01
Sigmoid function ν	42.132
Sigmoid function μ	0.327

weight is less than 5% as shown in Fig. 11 (b). The weight variation is more sensitive to the inductance error. Detailed percent errors in κ and ρ are summarized in Table 1.

V. EXPERIMENTAL RESULTS

Fig. 12 shows a test bench for experiments. The test motor parameters are listed in Table 2. The control board includes DSP TMS320F28377D and a 16-bit differential analog to digital converter (ADC). The PWM frequency is 5 kHz, whereas the current sampling frequency is 10 kHz. The deadtime is 2.5μs. The deadtime and IGBT on-drop were compensated to mitigate the inverter nonlinearity [20], [30], [31].

Fig. 13 shows a performance at 1000 rpm when the sensor signal is broken. The sensor fault is made just by stopping

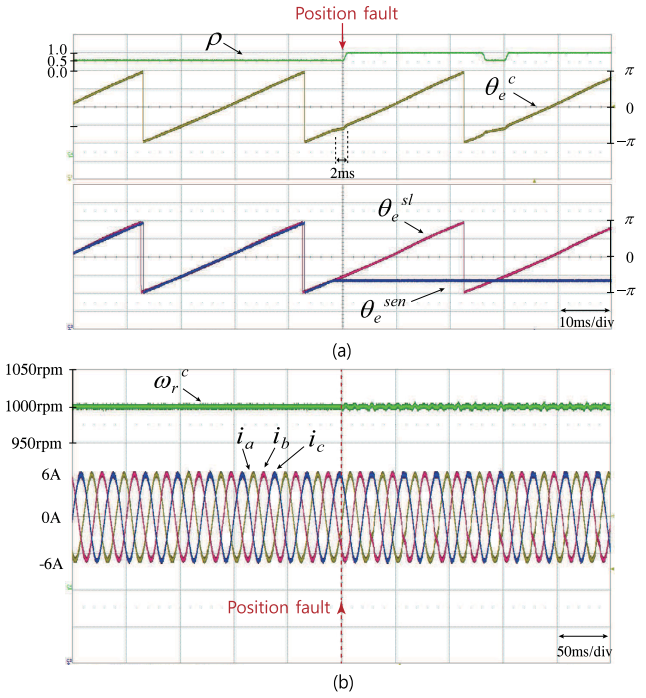

FIGURE 13. Experimental results of angle fusing at 1000 rpm under resolver sensor fault: (a) weight and angles, (b) speed and phase currents.

the resolver data refresh, thereby θ_e^{sen} remains constant in Fig. 13 (a). It causes a change in ρ to 1, meaning that the controller relies fully on the sensorless angle estimate. The failover algorithm is very smooth and fast, so it has almost no effect on current and speed. Note however that θ_e^{sl} hits the constant value θ_e^{sen} after one electrical cycle. Then, $\Delta\theta_e = 0$ again, so that ρ turns out to be $\frac{1}{2}$, and goes back to 1 afterwards. This causes a little distortion and ripple in current and speed, but stable speed control is sustainable.

Fig. 14 shows a recovery process when the position sensor fault is cleared during operation. In the bottom plot of Fig. 14 (a), θ_e^{sen} is back to normal from a constant. At that moment, ρ is changed from 1 to $\frac{1}{2}$, since both the sensored and sensorless signals are normal. Observe from the currents that there are slight current unsettling when ρ changes. It causes a little distortion in currents, but stable speed control is possible.

Fig. 15 shows a performance when the cosine resolver cable is shorted. Then, this causes θ_e^{sen} to be a rectangular signal. Even with this periodic error, the proposed algorithm works satisfactorily. Fig. 16 shows a similar result when the sine resolver cable is opened. In such a case, θ_e^{sen} turns out to be a sinusoidal wave. The algorithm also works satisfactorily.

The proposed algorithm is designed with the goal of operating for serious angle errors of about 15° or more. In practice, it is necessary to ensure that the algorithm does not malfunction due to load or parameter changes that may occur. Fig. 17 (a) shows the experimental results in which the resistance mismatch is changed from 20% to 50%. Because of the resistance mismatch, $\Delta\theta_e$ and sensorless angle errors

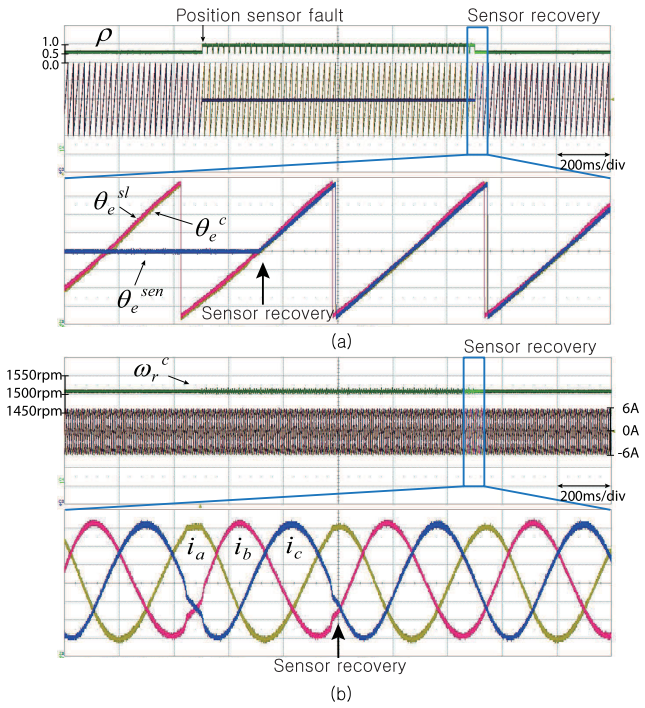

FIGURE 14. Experimental results of recovery process at 1500 rpm when sensor failure is cleared.

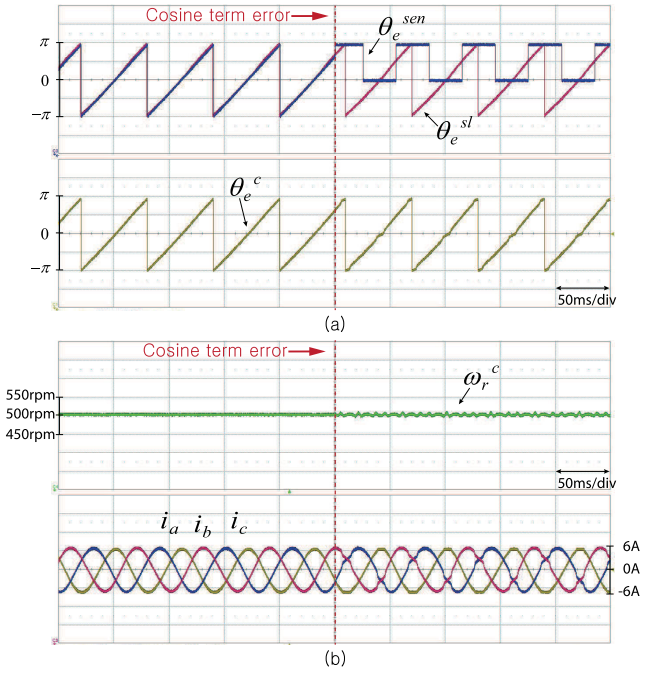

FIGURE 15. The proposed method according to V_{cos} fault (short error) at 500 rpm: (a) angles, (b) speed and phase currents.

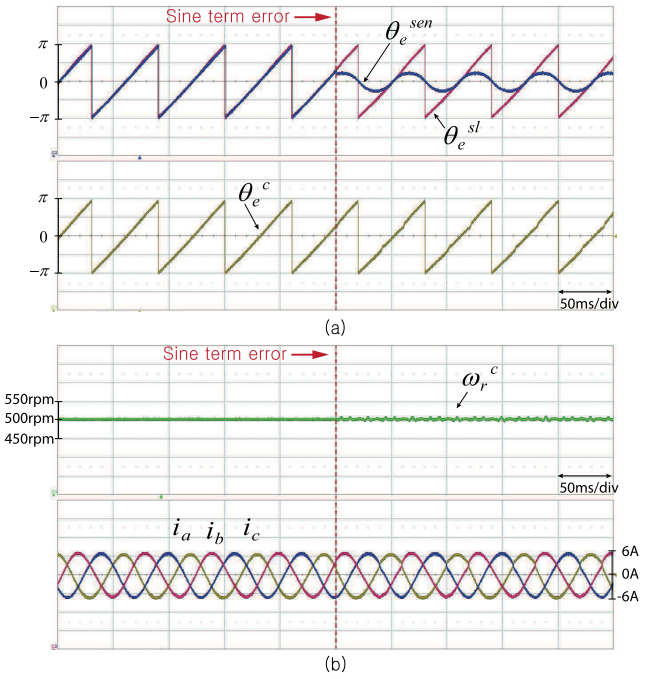

FIGURE 16. The proposed method according to V_{sin} fault (open error) at 500 rpm: (a) angles, (b) speed and phase currents.

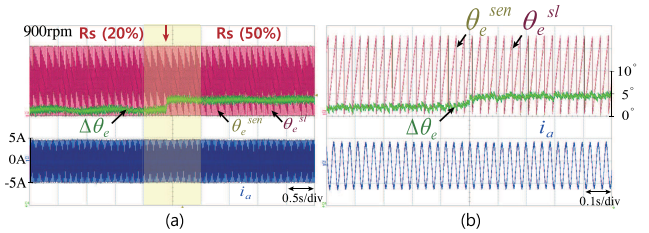

FIGURE 17. Effect due to resistance mismatch (20% to 50%).

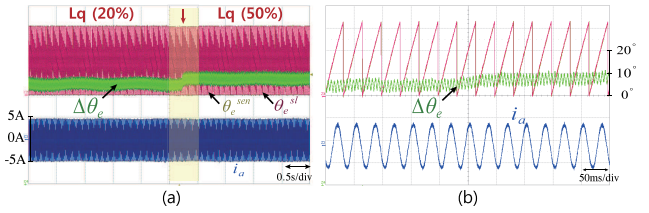

FIGURE 18. Effect due to *q*-axis inductance mismatch (20% to 50%).

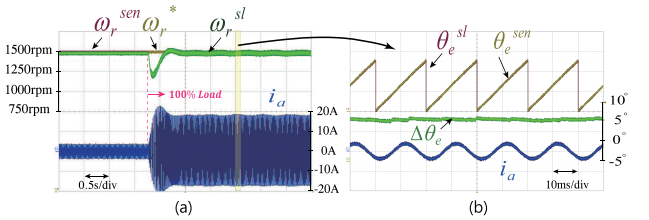

FIGURE 19. Experimental results at 1500 rpm with step load disturbance 100%.

increase. Fig. 17 (b), when the resistance mismatch is 50%, the angle error is 5° occurs. The algorithm does not work because it is not a value that is judged to be a severe error. Fig. 18 (a) and (b) show the experimental results in which the *q*-axis inductance mismatch is changed from 20% to 50%. Similarly, the angle error increases with the change in inductance, but it is not considered a failure. This algorithm

works for angle errors greater than about 15° degrees. It is not significantly affected by parameter mismatch. Fig. 19 (a) shows the result when the step load is 100% at 1500 rpm. $\Delta\theta_e$ is about 5°. It can be confirmed that there is no malfunction of the proposed algorithm due to the load.

VI. CONCLUSION

Sensored and sensorless methods are used in parallel to enhance the robustness of angle measurement. In the dual sensor system, there is no strict reference for detecting a fault and weighting the two angles. In this study, sensored and sensorless values are applied to the PMSM models as the angles of the reference frame. The virtual currents are obtained as the numerical solutions and compared to the real measured current. Among the two angles, an angle that generates a current close to the measured current is judged as an angle with a small error, and a fusing algorithm that gives a greater weight to a more accurate angle was created. Here, a sigmoid function with a holding region is used to make it insensitive to noise and small error fluctuations and to make a smooth transition. Therefore, a transition was made seamlessly if it completely depended on one sensing angle due to a failure. Simulation and experiments were carried out to demonstrate the validity of the algorithm. The main idea that utilizes mathematical models in the controller can be applied to the other multi-sensor systems as well.

REFERENCES

[1] A. P. Cohen, S. A. Shaheen, and E. M. Farrar, "Urban air mobility: History, ecosystem, market potential, and challenges," *IEEE Trans. Intell. Transp. Syst.*, vol. 22, no. 9, pp. 6074–6087, Sep. 2021, doi: 10.1109/TITS.2021.3082767.

[2] J. Lara, J. Xu, and A. Chandra, "Effects of rotor position error in the performance of field-oriented-controlled PMSM drives for electric vehicle traction applications," *IEEE Trans. Ind. Electron.*, vol. 63, no. 8, pp. 4738–4751, Aug. 2016.

[3] K. Wang and Z. Wu, "Oversampling synchronous envelope detection for resolver-to-digital conversion," *IEEE Trans. Ind. Electron.*, vol. 67, no. 6, pp. 4867–4876, Jun. 2020, doi: 10.1109/TIE.2019.2931250.

[4] K. Wang and Z. Wu, "Hardware-based synchronous envelope detection strategy for resolver supplied with external excitation generator," *IEEE Access*, vol. 7, pp. 20801–20810, 2019, doi: 10.1109/ACCESS.2019.2898466.

[5] D. Chen, J. Li, J. Chen, and R. Qu, "On-line compensation of resolver periodic error for PMSM drives," *IEEE Trans. Ind. Appl.*, vol. 55, no. 6, pp. 5990–6000, Nov. 2019.

[6] S. Wang, J. Kang, M. Degano, and G. Buticchi, "A resolver-to-digital conversion method based on third-order rational fraction polynomial approximation for PMSM control," *IEEE Trans. Ind. Electron.*, vol. 66, no. 8, pp. 6383–6392, Aug. 2019, doi: 10.1109/TIE.2018.2884209.

[7] K. Rothenhagen and F. W. Fuchs, "Doubly fed induction generator model-based sensor fault detection and control loop reconfiguration," *IEEE Trans. Ind. Electron.*, vol. 56, no. 10, pp. 4229–4238, Oct. 2009.

[8] G. H. B. Foo, X. Zhang, and D. M. Vilathgamuwa, "A sensor fault detection and isolation method in interior permanent-magnet synchronous motor drives based on an extended Kalman filter," *IEEE Trans. Ind. Electron.*, vol. 60, no. 8, pp. 3485–3495, Aug. 2013, doi: 10.1109/TIE.2013.2244537.

[9] F. Mwasilu and J.-W. Jung, "Enhanced fault-tolerant control of interior PMSMs based on an adaptive EKF for EV traction applications," *IEEE Trans. Power Electron.*, vol. 31, no. 8, pp. 5746–5758, Aug. 2016, doi: 10.1109/TPEL.2015.2495240.

[10] H. Berriri, M. W. Naouar, and I. Slama-Belkhodja, "Easy and fast sensor fault detection and isolation algorithm for electrical drives," *IEEE Trans. Power Electron.*, vol. 27, no. 2, pp. 490–499, Feb. 2012, doi: 10.1109/TPEL.2011.2140333.

[11] Y.-S. Jeong, S.-K. Sul, S. E. Schulz, and N. R. Patel, "Fault detection and fault-tolerant control of interior permanent-magnet motor drive system for electric vehicle," *IEEE Trans. Ind. Appl.*, vol. 41, no. 1, pp. 46–51, Jan. 2005, doi: 10.1109/TIA.2004.840947.

[12] D. Lee and K. Akatsu, "An improved position sensor fault detection and algorithm transition using adaptive threshold for sensorless control of IPMSM," in *Proc. 45th Annu. Conf. IEEE Ind. Electron. Soc.*, Oct. 2019, pp. 910–915.

[13] D. Lee and K. Akatsu, "The study on sensor fault detection and algorithm transition using adaptive threshold in position self-sensing control for IPMSM," *IEEE Trans. Ind. Electron.*, vol. 68, no. 11, pp. 10459–10466, Nov. 2021.

[14] J. Liu, T. A. Nondahl, J. Dai, S. Royak, and P. B. Schmidt, "A seamless transition scheme of position sensorless control in industrial permanent magnet motor drives with output filter and transformer for oil pump applications," *IEEE Trans. Ind. Appl.*, vol. 56, no. 3, pp. 2180–2189, May 2020, doi: 10.1109/TIA.2020.2977532.

[15] K. Lu, X. Lei, and F. Blaabjerg, "Artificial inductance concept to compensate nonlinear inductance effects in the back EMF-based sensorless control method for PMSM," *IEEE Trans. Energy Convers.*, vol. 28, no. 3, pp. 593–600, Sep. 2013.

[16] S.-C. Agarlita, I. Boldea, and F. Blaabjerg, "High-frequency-injection-assisted 'active-flu'-based sensorless vector control of reluctance synchronous motors, with experiments from zero speed," *IEEE Trans. Ind. Appl.*, vol. 48, no. 6, pp. 1931–1939, Nov. 2012, doi: 10.1109/TIA.2012.2226133.

[17] K. Nam, *AC Motor Control and Electric Vehicle Application*, 2nd ed. Boca Raton, FL, USA: CRC Press, 2018.

[18] L. D. Tornello, G. Scelba, G. Scarcella, M. Cacciato, A. Testa, S. Foti, S. de Caro, and M. Pulvirenti, "Combined rotor-position estimation and temperature monitoring in sensorless, synchronous reluctance motor drives," *IEEE Trans. Ind. Appl.*, vol. 55, no. 4, pp. 3851–3862, Jul. 2019, doi: 10.1109/TIA.2019.2915669.

[19] Y.-C. Kwon and S.-K. Sul, "Reduction of injection voltage in signal injection sensorless drives using a capacitor-integrated inverter," *IEEE Trans. Power Electron.*, vol. 32, no. 8, pp. 6261–6274, Aug. 2017, doi: 10.1109/TPEL.2016.2620259.

[20] L. M. Gong and Z. Q. Zhu, "A novel method for compensating inverter nonlinearity effects in carrier signal injection-based sensorless control from positive-sequence carrier current distortion," *IEEE Trans. Ind. Appl.*, vol. 47, no. 3, pp. 1283–1292, May/Jun. 2011, doi: 10.1109/TIA.2011.2128291.

[21] S.-K. Sul, Y.-C. Kwon, and Y. Lee, "Sensorless control of IPMSM for last 10 years and next 5 years," *CES Trans. Electr. Mach. Syst.*, vol. 1, no. 2, pp. 91–99, 2017.

[22] G. Zhang, G. Wang, and D. Xu, "Saliency-based position sensorless control methods for PMSM drives—A review," *Chin. J. Electr. Eng.*, vol. 3, no. 2, pp. 14–23, Sep. 2017.

[23] S. Morimoto, K. Kawamoto, M. Sanada, and Y. Takeda, "Sensorless control strategy for salient-pole PMSM based on extended EMF in rotating reference frame," *IEEE Trans. Ind. Appl.*, vol. 38, no. 4, pp. 1054–1061, Jul./Aug. 2002.

[24] F. Genduso, R. Miceli, C. Rando, and G. R. Galluzzo, "Back EMF sensorless-control algorithm for high-dynamic performance PMSM," *IEEE Trans. Ind. Electron.*, vol. 57, no. 6, pp. 2092–2100, Jun. 2010.

[25] D. Lee and K. Akatsu, "An improved speed and position estimator for transient performance of back-emf self-sensing for IPMSM," in *Proc. 44th Annu. Conf. IEEE Ind. Electron. Soc.*, Oct. 2018, pp. 397–402, doi: 10.1109/IECON.2018.8591825.

[26] J. Choi, K. Nam, A. A. Bobtsov, and R. Ortega, "Sensorless control of IPMSM based on regression model," *IEEE Trans. Power Electron.*, vol. 34, no. 9, pp. 9191–9201, Sep. 2019.

[27] A. Apte, V. A. Joshi, H. Mehta, and R. Walambe, "Disturbance-observer-based sensorless control of PMSM using integral state feedback controller," *IEEE Trans. Power Electron.*, vol. 35, no. 6, pp. 6082–6090, Jun. 2020.

[28] G. Wang, Z. Li, G. Zhang, Y. Yu, and D. Xu, "Quadrature PLL-based high-order sliding-mode observer for IPMSM sensorless control with online MTPA control strategy," *IEEE Trans. Energy Convers.*, vol. 28, no. 1, pp. 214–224, Mar. 2013, doi: 10.1109/TEC.2012.2228484.

[29] Y. G. Kang and D. D. Reigosa, "Dq-transformed error and current sensing error effects on self-sensing control," *IEEE J. Emerg. Sel. Topics Power Electron.*, early access, Jan. 18, 2021, doi: 10.1109/JESTPE.2021.3051942.

[30] Y. Park and S.-K. Sul, "A novel method utilizing trapezoidal voltage to compensate for inverter nonlinearity," *IEEE Trans. Power Electron.*, vol. 27, no. 12, pp. 4837–4846, Dec. 2012, doi: 10.1109/TPEL.2012.2192451.
[31] Z. Zhang and L. Xu, "Dead-time compensation of inverters considering snubber and parasitic capacitance," *IEEE Trans. Power Electron.*, vol. 29, no. 6, pp. 3179–3187, Jun. 2014, doi: 10.1109/TPEL.2013.2275551.

TAEYEON LEE was born in South Korea, in 1993. He received the B.S. degree in electrical engineering from Chungbuk National University, Cheongju, South Korea, in 2016, and the M.S. degree in electrical engineering from the Pohang University of Science and Technology (POSTECH), Pohang, South Korea, in 2018, where he is currently pursuing the Ph.D. degree.

His current research interests include AC motor control, electric vehicle, power electronic systems, and sensorless drive.

HEEKWANG LEE was born in Seoul, South Korea, in 1988. He received the B.S. degree in electrical engineering from Chungnam National University, Deajeon, South Korea, in 2012, and the Ph.D. degree in electrical engineering from the Pohang University of Science and Technology, Pohang, South Korea, in 2018.

He is currently a Research Engineer with Hyundai Motor R&D Center, Uiwang, South Korea. His research interests include the design, analysis, and control of power electronic systems, AC motor drive, and electric mobility.

POOREUM JANG was born in Yeosoo, South Korea, in 1993. He received the B.S. degree in electrical engineering from Pusan National University, Pusan, South Korea, in 2017, and the M.S. degree in electrical engineering from the Pohang University of Science and Technology (POSTECH), Pohang, South Korea, in 2019, where he is currently pursuing the Ph.D. degree.

His current research interests include AC motor control, electric vehicle, and power converter.

YUNKYUNG HWANG was born in Ulsan, South Korea, in 1992. He received the B.S. degree in energy engineering from Kyungpook National University, Daegu, South Korea, in 2018, and the M.S. degree in electrical engineering from the Pohang University of Science and Technology (POSTECH), Pohang, South Korea, in 2020, where he is currently pursuing the Ph.D. degree.

His current research interests include induction motor control, electric vehicle, and power electronics.

KWANGHEE NAM (Life Member, IEEE) received the B.S. degree in chemical technology and the M.S. degree in control and instrumentation engineering from Seoul National University, Seoul, South Korea, in 1980 and 1982, respectively, and the M.S. degree in mathematics and the Ph.D. degree in electrical engineering from the University of Texas at Austin, TX, USA, in 1986. From 1998 to 2000, he was the Director of the Information Research Laboratories and the Dean of the Graduate School of Information Technology, Pohang University of Science and Technology (POSTECH), Pohang, South Korea, where he is currently a Professor with the Department of Electrical Engineering. He actively involved in developing EV motors and inverters, since 1997, and led several big EV powertrain projects sponsored by major Korean companies. He acted as the Chair of IEEE supported international conferences, and is currently working as the President of the Korean Institute of Power Electronics (KIPE). He is the author of the book *AC Motor Control and Electrical Vehicle Applications*, (CRC Press, 2010). His current research interests include AC motor control, power converters, and motor design. He was a recipient of the Best Transaction Paper Award from the IEEE Industrial Electronics Society, in 2000, and the Second Best Paper Award at the 2014 IEEE Energy Conversion Congress and Exposition (ECCE).